JOURNAL OF SOLID STATE CHEMISTRY 59, 9–22 (1985)

Magnetic and Structural Properties of $Cr_{1-t}Ti_tAs$

HELMER FJELLVÅG AND ARNE KJEKSHUS

Department of Chemistry, University of Oslo, Blindern, N-0315 Oslo 3, Norway

Received August 6, 1984; in revised form October 28, 1984

The pseudobinary CrAs–TiAs system has been investigated by X-ray and neutron diffraction and magnetic susceptibility measurements at temperatures between 10 and 1000 K. The phase diagram includes paramagnetic regions with the MnP-, NiAs-, and TiP-type structures and a low-temperature helimagnetic, MnP-type state for $0.00 \leqq t \leqq 0.10$ of $Cr_{1-t}Ti_tAs$. The first-order para- to helimagnetic transition in $Cr_{1-t}Ti_tAs$ is accompanied by a hysteresis of 10–15 K. The results are discussed in relation to the findings for other $Cr_{1-t}T_tAs$ (T = V, Mn, Fe, Co, Ni) and $CrAs_{1-x}X_x$ (X = P, Sb, Se) phases.

Introduction

CrAs is an interesting member of both the MnP- and NiAs-type families [cf., e.g., (*1*, *2*) and references therein]. Features which attract attention are:

(i) The second or higher order MnP ⇄ NiAs-type transition at $T_D = 1173 \pm 20$ K. This transition extends into the ternary ranges of the solid solution phases $Cr_{1-t}T_tAs$ [T = V (*3*), Mn (*4*, *5*), Fe (*6*), Co (*7*), Ni (*8*)] and $CrAs_{1-x}X_x$ [X = P (*9*)], but hitherto only $Cr_{1-t}Mn_tAs$ has disclosed an appreciable variation of T_D with t.

(ii) The helimagnetic (H_c) phase of the so-called double c axis type (*1*, *10*) at low temperatures; also, the H_c phase spread out into $Cr_{1-t}T_tAs$ (*3–8*) and $CrAs_{1-x}X_x$ (*9*, *11*). However, apart from $Cr_{1-t}Mn_tAs$ (*4*, *12*) and $CrAs_{1-x}Sb_x$ (*11*) the H_c arrangement breaks down for rather low values of t or x.

(iii) The paramagnetic (P) to H_c transition is of first order with hysteresis (*1*, *10*, *11*, *13–15*). There are some disagreements about the value for the Néel temperature on cooling ($T_{N,c}$) and heating ($T_{N,h}$), but 261 and 272 K, respectively, reported by Selte *et al.* (*1*), are self-consistent with those in this communication. The first-order character of the P to H_c transition is also maintained in $Cr_{1-t}T_tAs$ and $CrAs_{1-x}X_x$. For $Cr_{1-t}Mn_tAs$ the P to H_c transition converts to second order at $t \geqq 0.10$ (*5*).

The present paper concerns structural and magnetic properties of the CrAs–TiAs system. Only rather sparse information on this system is available in the literature (*16*, *17*).

Experimental

CrAs and TiAs were synthesized according to the sealed silica capsule technique as described in (*12*, *18*). Weighed amounts of CrAs and TiAs, in the desired proportions, were heated at 1000°C for 5 days. After careful grinding the samples were subject to two further, similar annealings and finally the samples were slowly cooled to room temperature over 1 day. The homogeneity of the samples was ascertained by room-temperature powder X-ray (Guinier) dif-

0022-4596/85 $3.00

fraction [(Cu$K\alpha_1$ radiation, λ = 154.0598 pm; Si as internal standard, a = 543.1065 pm (*19*)]. Low- and high-temperature X-ray diffraction photographs were obtained in a Guinier Simon camera (Enraf–Nonius). The sample was kept in a rotating, sealed silica capillary, and the temperature could be varied continuously between 100 and 1300 K. The temperature difference between the programmed temperature and that of the sample is estimated to be less than 5 K at 1300 K.

Magnetic susceptibilities were measured between 80 and 1000 K by the Faraday method (maximum field ~8 kOe, samples of 10–20 mg).

Powder neutron diffraction diagrams were recorded with the OPUS III spectrometer at the JEEP II reactor, Kjeller, using neutrons of wavelength 187.7 pm. Temperatures between 10 and 300 K were attained with a Displex cooling device. The Hewat (*20*) version of the Rietveld (*21*) program was used in the profile refinements of the powder neutron diffraction data. The scattering lengths (in 10^{-12} cm) b_{Cr} = 0.352, b_{Ti} = −0.34 and b_{As} = 0.64 were taken from the compilation in (*22*), and the magnetic form factor for Cr^{3+} from (*23*).

Results

(*i*) *Atomic arrangement.* CrAs takes the MnP-type structure (here using the *Pnma* setting, $c > a > b$) up to T_D = 1173 ± 20 K where it converts to the NiAs type. At room temperature the MnP-type structure prevails for $Cr_{1-t}Ti_tAs$ with $0.00 \leqq t <$ ~0.40. The binary end phase TiAs takes the TiP-type structure, which is closely related to the NiAs type (*24*). For $Cr_{1-t}Ti_tAs$ the TiP-type structure is found for 0.97 ± 0.02 $\leqq t \leqq$ 1.00, viz., in a narrow region near TiAs. The NiAs-type structure occurs in the interval ~0.40 $\leqq t \leqq$ 0.90, and a narrow miscibility gap, 0.93 ± 0.02 $\leqq t \leqq$ 0.97 ± 0.02, separates the NiAs- and TiP-type

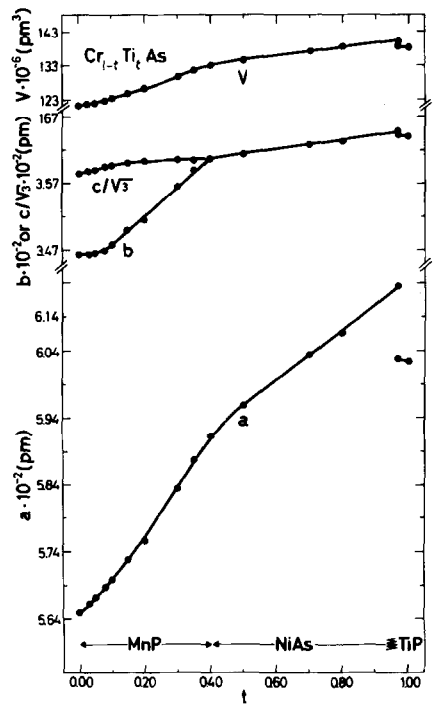

FIG. 1. Unit-cell dimensions of $Cr_{1-t}Ti_tAs$ at 293 K. *Calculated* error limits do not exceed size of symbols. Structural state is indicated at the bottom of the illustration. (1 Å = 10^2 pm.)

phase regions. The variations in the unit-cell dimensions of $Cr_{1-t}Ti_tAs$ (for slowly cooled samples) with the compositional parameter t at 293 K (Fig. 1) reflect these phase relations.

Boller *et al.* (*16, 17*) report two modifications of TiAs. In order to verify the claimed high-temperature, NiAs-type modification, TiAs was examined by the high-temperature X-ray technique. However, no TiP- to NiAs- (nor any other) type phase transition was detected at temperatures below ~1370 K. Only samples with a Ti : As atomic ratio of 1 : 1 were subject to this study, and the possibility that nonstoichiometric TiAs may take the NiAs-type structure (at elevated temperatures) is accordingly still open. The temperature dependence of the unit-cell dimensions for TiAs is depicted in Fig. 2.

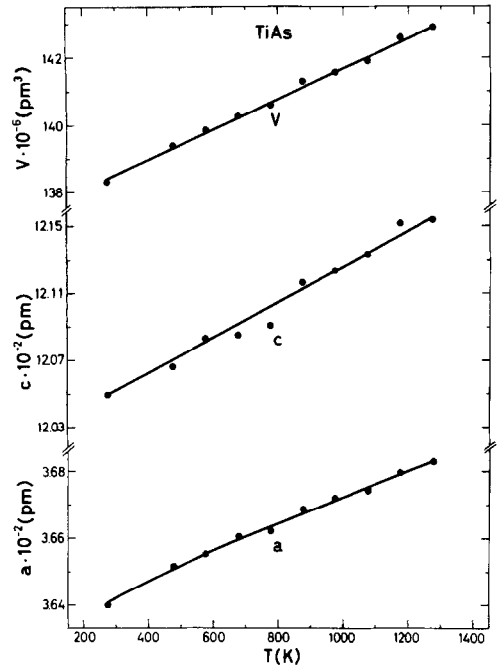

FIG. 2. Thermal expansion of TiAs 273–1273 K. *Calculated* error limits do not exceed twice the size of symbol. (1 Å = 10^2 pm.)

The (orthorhombic) MnP-type structure is a variant of the (hexagonal) NiAs type ($\mathbf{a}_{MnP} = \mathbf{c}_{NiAs}$; $\mathbf{b}_{MnP} = \mathbf{b}_{NiAs}$; $\mathbf{c}_{MnP} = 2\mathbf{a}_{NiAs} + \mathbf{b}_{NiAs}$). The metal and nonmetal atoms are, relative to their positions in the NiAs-type structure, displaced mainly parallel to c_{MnP} and a_{MnP}, respectively (*2*). The MnP- to NiAs-type phase transition is, according to symmetry considerations on the basis of Landau theory, allowed to be of the continuous, second-order type (*25*). This feature has now been verified experimentally for many binary and ternary representatives of the MnP-type family, e.g., $Mn_{1-t}T_tAs$ (*2, 8, 12, 18, 26–28*), $MnAs_{1-x}X_x$ (*29, 30*), $Cr_{1-t}T_tAs$ (*3, 5–8*), and $CrAs_{1-x}X_x$ (*9*).

In ternary solid-solution systems where the binary end phases take, respectively, the MnP- and NiAs-type structures, one may expect that T_D for the MnP ⇄ NiAs-type transition varies continuously with the compositional parameter (t or x) and finally approaches zero for a certain value of t or x [cf. (*4, 18, 31*)]. However, the MnP- and NiAs-type phases of such systems are often separated by a two-phase region, which, e.g., is the case for $Cr_{1-t}V_tP$, (*32*), $Mn_{1-t}Fe_tAs$ (*33*), $Cr_{1-t}Ni_tAs$ (*8*), $CoAs_{1-x}Sb_x$ (*34*), and $VP_{1-x}As_x$ (*35*). (In the latter case there also occurs an intermediate ternary phase with a distinct structure.)

According to Fig. 1, $Cr_{1-t}Ti_tAs$ is a strong candidate for the feature "continuous variation in T_D with t". The MnP ⇄ NiAs-type phase transition is clearly revealed in high- or low-temperature X-ray diffraction photographs and in the magnetic susceptibility data [see (ii)] of $Cr_{1-t}Ti_tAs$. For $0.00 \leqq t \leqq 0.35$, T_D was found to be above room temperature; for $t = 0.40$, below this temperature; and for $t = 0.45$, no sign of any phase transition was observed above 100 K. (The unit-cell dimensions for $t = 0.45$ (NiAs type) vary linearly between

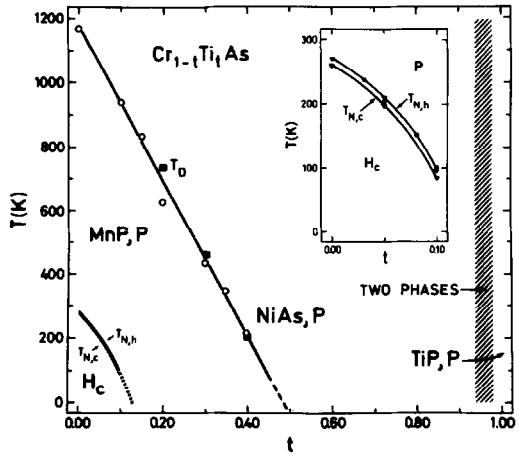

FIG. 3. Phase diagram for the pseudobinary CrAs–TiAs system. Structural state is indicated by type designation, magnetic state by H_c (c-axis helical) and P (para). T_D denotes the MnP,P ⇄ NiAs,P-type (distortion) transition, and $T_{N,h}$ and $T_{N,c}$ distinguish the Néel temperature on heating and cooling, respectively. Results marked ■ are obtained from magnetic susceptibility; ○, ● by X-ray; and ▽, ▼ by neutron diffraction measurements. Data for CrAs are quoted from (*1*).

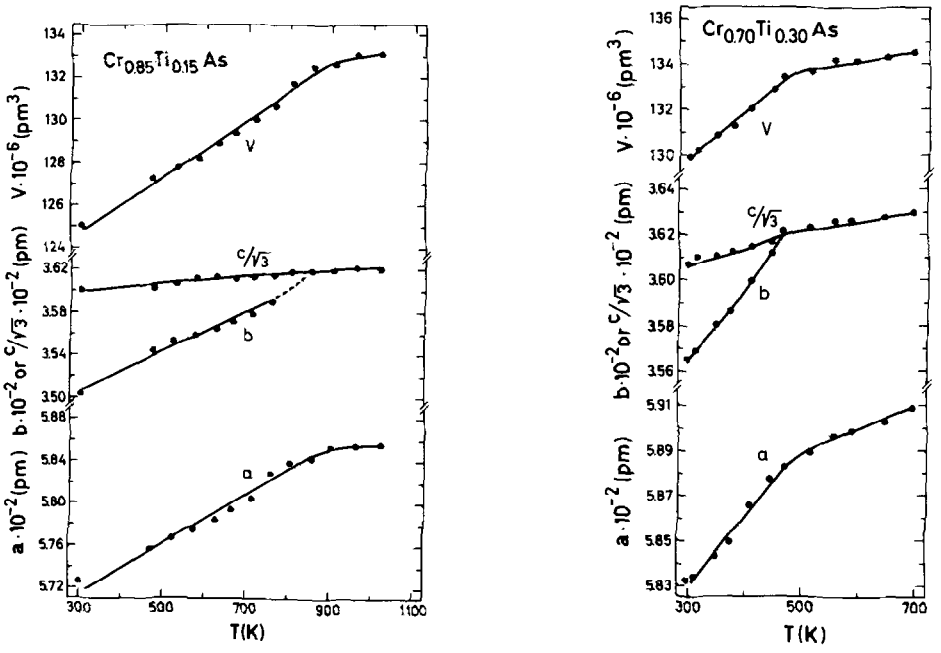

FIG. 4. Thermal expansion of $Cr_{0.85}Ti_{0.15}As$ and $Cr_{0.70}Ti_{0.30}As$. *Calculated* error limits do not exceed twice the size of symbol. (1 Å = 10^2 pm.)

$a = 360.6 \pm 0.1$ pm, $c = 591.3 \pm 0.1$ pm at 90 K, and $a = 361.0 \pm 0.1$ pm, $c = 592.9 \pm 0.1$ pm at 293 K.) T_D was obtained by visual inspection of the X-ray diffraction photographs. As seen from the phase diagram of $Cr_{1-t}Ti_tAs$ in Fig. 3, T_D decreases almost linearly with t, passes through 293 K at $t \approx 0.37$ (see also Fig. 1), and approaches zero at $t \approx 0.50$. The approximately linear T_D-versus-t relationship for $Cr_{1-t}Ti_tAs$ resembles the findings for $Mn_{1-t}Cr_tAs$ (*4*, *5*). The thermal expansion curves for the unit-cell dimensions of $Cr_{1-t}Ti_tAs$ with $t = 0.15$ and 0.30 (Fig. 4) may serve as representative examples of the present results.

Crystallographic data for $Cr_{1-t}Ti_tAs$ with $t = 0.05$ and 0.10 at 10 and 293 K, as derived by Rietveld analyses of powder neutron diffraction data, are listed in Table I. The evaluation is based on the assumption that the long-range distribution of Cr and Ti is random over the metal sublattice. (This

TABLE I

UNIT-CELL DIMENSIONS AND POSITIONAL PARAMETERS WITH STANDARD DEVIATIONS FOR $Cr_{1-t}Ti_tAs$ AS DERIVED BY RIETVELD ANALYSIS OF POWDER NEUTRON DIFFRACTION DATA

t	T(K)	a(pm)	b(pm)	c(pm)	x_T	z_T	x_{As}	z_{As}
0.05	293	567.32(5)	347.15(2)	621.90(4)	0.0063(18)	0.2008(13)	0.2025(7)	0.5763(8)
	10	563.61(4)	357.74(4)	615.54(6)	0.0091(10)	0.2013(7)	0.2061(3)	0.5798(8)
0.10	293	569.78(5)	347.79(2)	622.96(4)	0.0026(23)	0.2010(16)	0.2042(8)	0.5770(9)
	10	566.54(7)	356.30(8)	617.77(9)	0.0020(40)	0.2043(34)	0.2056(13)	0.5750(39)

Note. Space group *Pnma*; Cr/Ti in 4*c* and As in 4*c*. (Nuclear R_n factors ranging between 0.03 and 0.05; profile R_p factors ranging between 0.08 and 0.11; 25–30 nuclear reflections.)

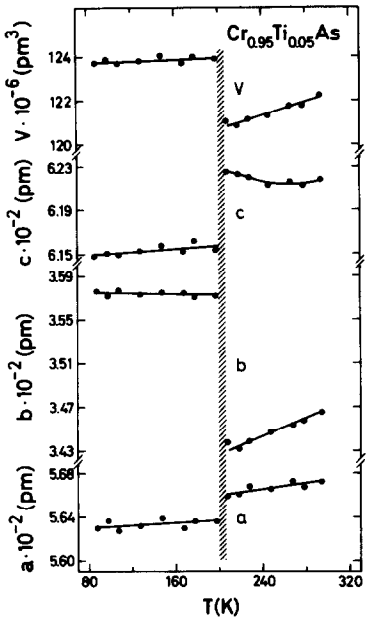

FIG. 5. Thermal expansion of $Cr_{0.95}Ti_{0.05}As$ 90–300 K (on heating). *Calculated* error limits do not exceed twice the size of symbol. Hysteresis region of the MnP,H_c- to MnP,P-type transition is hatched. (1 Å = 10^2 pm.)

assumption is supported by sharp Bragg reflections, lack of additional superstructure reflections, and generally good fit between observed and calculated neutron diffraction intensities.) Only minor variations in the positional parameters occur with t and T. On the other hand, for a given composition there are large differences between the unit-cell dimensions at 10 and 293 K. This is due to the coupled structural and magnetic phase transition at the P to H_c phase transition [see (iii)].

The first-order P to H_c transition (at T_N) is clearly reflected in the thermal expansion of the unit-cell dimensions of $Cr_{1-t}Ti_tAs$ with $0.00 \leqq t \leqq 0.10$. The results for $Cr_{0.95}Ti_{0.05}As$ (Fig. 5) give a representative example. The transition temperatures found by X-ray diffraction ($T_{N,h}$ = 235 ± 5, 205 ± 5, 150 ± 5 and 100 ± 5 K for t = 0.03, 0.05, 0.08 and 0.10, respectively) are in excellent agreement with those derived by neutron diffraction (cf. Fig. 3 and vide infra).

In order to establish whether or not the structural and magnetic phase transitions coincide in temperature, nuclear and magnetic reflections were recorded simultaneously by powder neutron diffraction. The integrated intensity-versus-temperature relationships for t = 0.05 and 0.10 (Fig. 6) reveal (within the estimated error limits of the experiments) no distinction between the nuclear and magnetic reflections in this respect. The conclusion is accordingly that

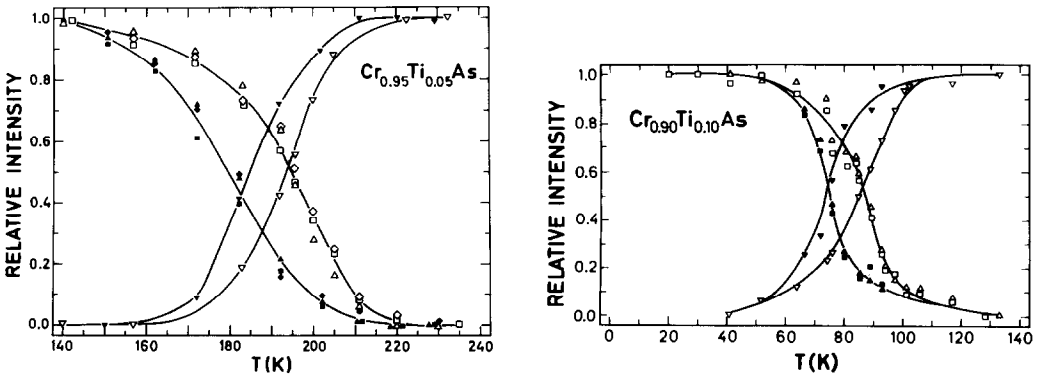

FIG. 6. Relative integrated intensity of nuclear and magnetic reflections versus temperature for $Cr_{0.95}Ti_{0.05}As$ and $Cr_{0.90}Ti_{0.10}As$. Open and filled symbols refer to data obtained upon heating and cooling, respectively. Results marked △, ▲ refer to 111 plus 102 (nuclear); ▽, ▼ to 112 (nuclear); □, ■ to $000^{\pm}$ (magnetic); and ◇, ◆ to 101^{-} (magnetic).

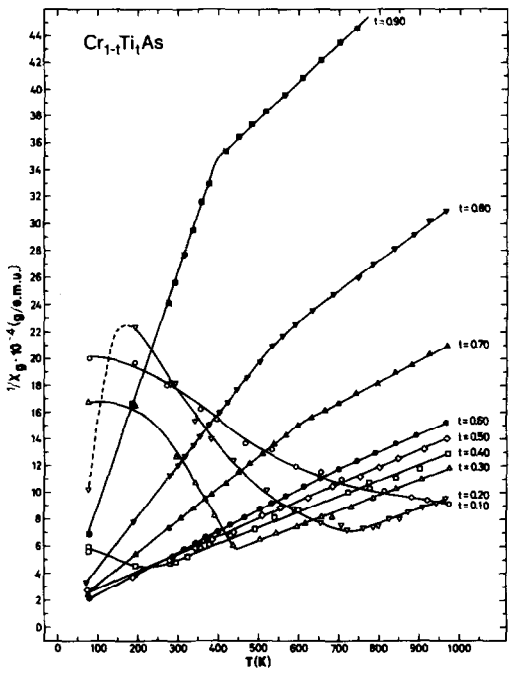

FIG. 7. Inverse magnetic susceptibility as function of temperature for $Cr_{1-t}Ti_tAs$ with $t = 0.10, 0.20, 0.30, 0.40, 0.50, 0.60, 0.70, 0.80$, and 0.90.

the structural and magnetic changes at this MnP(I),P- to MnP(II),H_c-type transition are fully coupled (viz., inseparable). $T_{N,h}$ = 212 ± 5 and 96 ± 5 K and $T_{N,c}$ = 200 ± 5 and 84 ± 5 K are estimated for $t = 0.05$ and 0.10, respectively.

(ii) Magnetic susceptibility. The reciprocal magnetic susceptibility-versus-temperature curves for $Cr_{1-t}Ti_tAs$ with $0.10 \leqq t \leqq 0.80$ are shown in Fig. 7. On comparing Figs. 3 and 7 it is evident that linear sections of the $\chi^{-1}(T)$ curves are connected with the NiAs,P-type state. Hence, the Curie–Weiss law $[\chi^{-1} = C^{-1}(T - \theta)]$ is fulfilled for the NiAs,P-type state as opposed to for the MnP,P-type state. The nonlinear behaviors of the $\chi^{-1}(T)$ curves in the MnP,P-type state are probably inter alia a reflection of a gradual reduction in the number of unpaired electrons and/or changes in the magnitude of the exchange interactions with decreasing temperature (*35*). However, effects of a progressive MnP-type crystallographic deformation [cf. (*2, 25*) and vide infra] on the electronic band struc-

TABLE II

WEISS CONSTANT (θ), PARAMAGNETIC MOMENT (μ_{eff}), AND NUMBER OF UNPAIRED SPINS ($2S$) FOR THE NiAs,P-TYPE STATE OF $Cr_{1-t}Ti_tAs$

t	θ(K)	μ_{eff}(μ_B per Cr/Ti)	$2S$(per Cr/Ti)	T_D(K)	Curie–Weiss region (K)
0.00	—	—	—	>1000	
0.10	—	—	—	>1000	
0.20	50 ± 25	3.08 ± 0.10	2.24 ± 0.07	735 ± 15	735–1000
0.30	−55 ± 15	2.98 ± 0.05	2.14 ± 0.03	440 ± 10	440–1000
0.40	−110 ± 10	2.91 ± 0.05	2.07 ± 0.03	230 ± 25	230–1000
0.50	−140 ± 15	2.79 ± 0.05	1.97 ± 0.03	<80	80–1000
0.60	−50 ± 10	2.52 ± 0.08	1.71 ± 0.06	—	80–700
	−310 ± 30	2.77 ± 0.12	1.96 ± 0.09		700–1000
0.70	−30 ± 10	2.05 ± 0.08	1.28 ± 0.06	—	80–600
	−430 ± 40	2.47 ± 0.08	1.67 ± 0.06		600–1000
0.80	−15 ± 10	1.64 ± 0.08	0.92 ± 0.06	—	80–550
	−520 ± 50	2.12 ± 0.08	1.34 ± 0.06		550–1000
0.90	−10 ± 10	1.08 ± 0.10	0.47 ± 0.08	—	80–400
	−900 ± 70	1.89 ± 0.08	1.14 ± 0.06		400–1000

Note. The MnP,P ⇄ NiAs,P-type transition temperature (T_D), as derived from magnetic susceptibility data, is included.

ture of $Cr_{1-t}T_tAs$ and $Mn_{1-t}T_tAs$ will be discussed elsewhere. As seen from Fig. 3, the T_D values derived from the kink points on the $\chi^{-1}(T)$ curves closely match those obtained by the X-ray diffraction method.

For $0.20 \leqq t \leqq 0.50$, $\chi^{-1}(T)$ satisfies the Curie–Weiss law for $T_D < T < \sim 1000$ K (probably over the entire temperature range of the NiAs,P-type state). The linear $\chi^{-1}(T)$ characteristics for $0.60 \leqq t \leqq 0.90$ convert to curves which are slightly concave toward the temperature axis on the high-temperature side. As seen from Fig. 7, the latter feature becomes gradually more pronounced when t increases. This trend resembles the findings for, e.g., the $Mn_{1-t}T_tP$ phases, and will be discussed elsewhere (*35*).

The paramagnetic moments ($\mu_{eff} = \sqrt{8C_{mol}}$) and Weiss constants ($\theta$) are given in Table II together with the corresponding number of unpaired spins ($2S$) according to the "spin only" approximation [$\mu_{eff} = g\sqrt{S(S+1)}$ with $g = 2$]. The χ^{-1} curves for $0.60 \leqq t \leqq 0.90$ have been approximated by two Curie–Weiss law relationships, for which the data listed for "high-temperature Curie–Weiss regions" in Table II most likely have no simple physical interpretation. (Careful examination of high-temperature Guinier–Simon X-ray photographs shows that this behavior is not correlated with any crystallographic change.)

μ_{eff} and $2S$ decrease with increasing t, and θ does the same up to $t = 0.50$, where it goes through a slight minimum and approaches 0 K. This is depicted in Fig. 8, which also shows the relations between, respectively, $2S$, θ and μ_H, T_N [the two latter derived by neutron diffraction, see (iii)]. The illustration brings out a fairly close correspondence between θ and T_N and a very marked difference between $2S$ and μ_H. Since the two sets of data refer to the quite different NiAs,P- and MnP,H_c-type states, the resemblance between the former pair of parameters appears more remarkable than

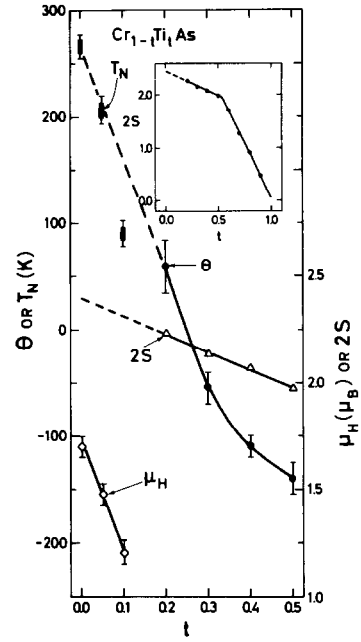

FIG. 8. $2S$ ("spin only") and θ values from magnetic susceptibility and μ_H and T_N values from neutron diffraction versus the compositional parameter t of $Cr_{1-t}Ti_tAs$. Legends to symbols are given on the illustration. Bars represent estimated or calculated errors.

the distinction between the latter. Some of the disparity in $2S$ and μ_H may be attributed to a difference in methodology (magnetic susceptibility versus neutron diffraction), but we assume (*35*) that the major part originates from the gradual reduction in the number of unpaired spins with the progressive MnP-type crystallographic deformation (vide infra).

The change in the slope of the $2S$-versus-t relationship at $t \approx 0.55$) in the inset to Fig. 8 is correlated with the nonlinear behavior of $\chi^{-1}(T)$ in the NiAs,P-type state (vide supra). These features are different reflections of a parallel alteration of the electronic band structure with t. $2S$ extrapolates (cf. Fig. 8) to ~2.4 for $t = 0.00$ (viz., CrAs) and ~0.0 for $t = 1.00$ (viz., TiAs), the latter finding being consistent with the magnetic properties reported for TiAs (*17*) itself.

TABLE III
HELIMAGNETIC PARAMETERS FOR $Cr_{1-t}Ti_tAs$ AT 10 K

t	$\tau_c/2\pi c^*$	$\mu_H(\mu_B)$	$\phi_{1,2}(°)$
0.00	0.353 ± 0.002	1.70 ± 0.05	−133 ± 1
0.05	0.378 ± 0.002	1.48 ± 0.05	−122 ± 3
0.10	0.396 ± 0.002	1.21 ± 0.05	−124 ± 3

Note. R_{spiral} ranging between 0.03 and 0.08; 8–11 magnetic satellite reflections. Data for CrAs are quoted from (*1*).

(*iii*) *Magnetic structures.* The magnetic phase relationships in the CrAs–TiAs system are summarized in Fig. 3. The TiP- and NiAs-type phases are consistently in a P state, whereas MnP(I),P converts into MnP(II),H_c for $T < T_N$ ($T_{N,c}$ or $T_{N,h}$ depending on cooling or heating conditions) and $0.00 \leqq t \leqq 0.10$. The width of the hysteresis loops for the MnP(I),P- to MnP(II),H_c-type transition [see (i)] is approximately constant (ΔT_N = 10–15 K) over the composition interval concerned. [The large scatter in the T_N values reported (*1, 10, 11, 13–15*) for CrAs probably originates to a large extent from differences in the procedures for sample preparation. Melting may, e.g., produce some (difficult controlled) variation in $T:X$ stoichiometry and solid-state reactions are, e.g., likely to introduce (temperature-dependent) appreciable, and probably fluctuating degrees of short-range order. The present preparational procedure is compatible with those of (*1, 15*).]

For CrAs (*1, 10*), $Cr_{1-t}T_tAs$ (*3–8*), and $CrAs_{1-x}X_x$ (*9, 11*) a magnetic structure similar to that (*36, 37*) originally proposed for MnP has proved to represent a reasonable approximation, and hence this model is also adopted for $Cr_{1-t}Ti_tAs$. Numerical values for the variable parameters of the model [viz., the propagation vector τ_c of the spirals, the helimagnetic moment μ_H and the phase angle $\phi_{1,2}$ between the spirals through atoms 1 and 2, cf. (*12*)] are given in Table III, which also includes the corresponding data for CrAs quoted from (*1*). τ_c increases slightly with increasing t and is essentially independent of T, and $\phi_{1,2}$ changes very little with both t and T. μ_H, on the other hand, decreases appreciably with increasing t and T ($\mu_H = 0\ \mu_B$ at T_N).

Discussion

Information on the structural and magnetic properties of $Cr_{1-t}T_tAs$ with T = Ti–Ni and $CrAs_{1-x}X_x$ with X = P, Sb, Se are now at hand. Hence, it seems pertinent to systematize these data and relate them to the properties of CrAs itself.

Phase diagram data for $Cr_{1-t}T_tAs$ and $CrAs_{1-x}X_x$ are summarized in Fig. 9. The MnP ⇄ NiAs-type crystallographic tran-

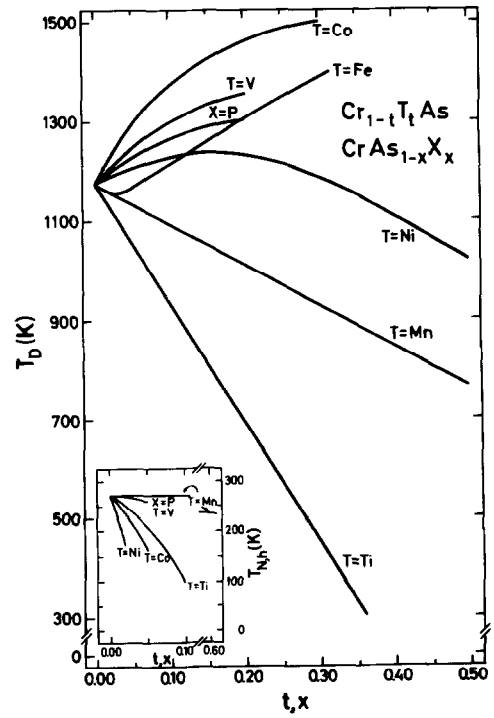

FIG. 9. Phase diagram data for $Cr_{1-t}T_tAs$ and $CrAs_{1-x}X_x$. T_D refers to the NiAs,P ⇄ MnP,P-type transition, T_N to the MnP(I),P- to MnP(II),H_c-type transition, and indices c and h to cooling and heating conditions, respectively. Data from (*1, 3–12*).

sition is retained over appreciable composition regions of the ternary phases. The T_D-versus-t or -x relationships for the different T or X substituents (Fig. 9) may be divided in three broad categories according to whether T_D increases (T = V, Fe, Co; X = P), remains roughly constant (T = Ni with willful suppression of facts), or decreases (T = Ti, Mn) with increasing t or x. $CrAs_{1-x}X_x$ with X = Sb, Se almost certainly belongs to the latter category [cf. (*11*, *38*)], but only scattered phase diagram data are available. The trends in T_D versus t or x are, except perhaps for T = Co, Ni, consistent with expectations on the basis of the structural state and stability of the corresponding TAs and CrX end phases. An extrapolation of T_D for $Cr_{1-t}Ni_tAs$ to NiAs is certainly questionable in view of the miscibility gap in the CrAs–NiAs system (*8*). With T_D = 1250 K for CoAs (*2*), Fig. 9 suggests that T_D versus t for $Cr_{1-t}Co_tAs$ goes through a maximum (tentatively at $t \approx 0.5$, $T_D \approx 1500$ K).

The magnetic portions of the phase diagrams for $Cr_{1-t}T_tAs$ and $CrAs_{1-x}X_x$ are similarly compressed in the inset to Fig. 9. The hysteresis-accompanied MnP(I),P- to MnP(II),H_c-type transition is common to all these phases. The H_c mode usually breaks down already at a substitution level of 0.05–0.10 in t or x. $Cr_{1-t}Mn_tAs$ represents a notable exception with a stability range ($0.00 \leqq t \leqq 0.65$) for the H_c mode (*12*). $CrAs_{1-x}Sb_x$, which is similar (with a stability range of $0.00 \leqq x \leqq 0.59$), has not been included because of some disparity in T_N for CrAs itself in the study concerned (*11*).

The origin of the crystallographic rearrangement at the MnP(I),P- to MnP(II),H_c-type transition in the $Cr_{1-t}T_tAs$ and $CrAs_{1-x}X_x$ phases is an intricate problem. A natural starting point for some considerations on the problem is the experimental fact that the positional parameters of the MnP-type structure remain virtually unchanged at this transition [see (i) and (*1*, *3*, *5–9*)].

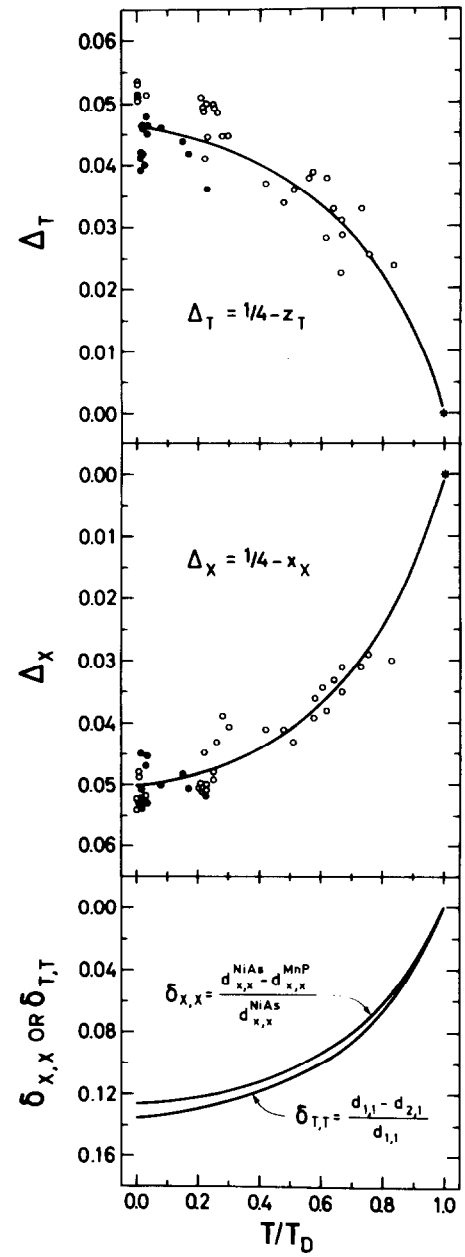

FIG. 10. Variations in the displacement-adapted parameters $\Delta_T = \frac{1}{4} - z_T$ and $\Delta_X = \frac{1}{4} - x_X$ for the MnP-type structure as function of reduced temperature (T/T_D); where T_D refer to the NiAs,P ⇄ MnP,P-type transition. Relative changes in second shortest T–T ($d_{2,1}$) and shortest X–X ($d_{X,X}$) distances with T/T_D. $d_{1,1} = b$ corresponds to the third shortest T–T distance. Open and filled symbols in the upper parts refer to paramagnetic and cooperative magnetic states, respectively.

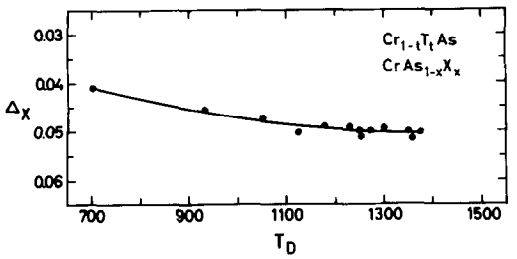

FIG. 11. T_D versus $\Delta_X = \frac{1}{4} - x_X$ for $Cr_{1-t}T_tAs$ and $CrAs_{1-x}X_x$ phases.

The distortion from NiAs- to MnP-type structure is [cf. (*2*, *25*, *26*)] characterized by gradual displacements of the T and X atoms from their NiAs-type (fixed) positions as a function of temperature. In terms of an MnP-type description for both structures the most significant atomic shifts involve the parameters z_T and x_X (which are an order of magnitude larger than the changes in x_T and z_X). $\Delta_T = \frac{1}{4} - z_T$ and $\Delta_X = \frac{1}{4} - x_X$ may be taken as measures for how far the MnP-type deformation has progressed. ($\Delta_T = \Delta_X = 0$ corresponds to the NiAs-type structure.) Δ_T and Δ_X versus T/T_D for phases which undergo the NiAs⇄MnP-type transition are presented in Fig. 10, and to a passable approximation the data points may be represented by the solid curves. (The scatter in the data points for Δ_T is as expected somewhat larger than for Δ_X.) When Δ_T and Δ_X increase the second shortest T–T distance ($d_{2,1}$) and the shortest X–X distance ($d_{X,X}$) decrease. This is illustrated in the lower part of Fig. 10 where the relative variations in $d_{2,1}$ and $d_{X,X}$ with T/T_D are depicted (for CrAs; the scale is slightly different for other model substances). [Apart from $d_{1,1} = b$ which corresponds to the third shortest T–T distance in the MnP-type structure, the notations introduced on the illustration should be self-explanatory.]

The object of this slight digression has been to demonstrate that the different curves of Fig. 10 take a rather uniform shape. Despite the true multidimensional nature of the NiAs⇄MnP-type transition any of the four parameters (Δ_T, Δ_X, $\delta_{X,X}$, and $\delta_{T,T}$) in Fig. 10 (and probably others in addition) can be chosen as an indicator of the degree of MnP-type deformation, viz., as a single, "independent" deformation parameter. In line with this, Fig. 11 presents a close correlation between T_D and $\frac{1}{4} - x_X = \Delta_X$ for the $Cr_{1-t}T_tAs$ and $CrAs_{1-x}X_x$ phases.

Returning to the MnP(I),P- to MnP(II), H_c-type transition in the $Cr_{1-t}T_tAs$ and $CrAs_{1-x}X_x$ phases, the T_N/T_D values in the range 0.10 and 0.25 suggest that some, although not large, changes in the positional parameters are permitted within the correlation schemes advanced in Fig. 10. (The freedom for adjustments of the positional parameters will clearly be considerably larger if the full ranges covered by the data points in Fig. 10 are taken into account.) Nevertheless, the crystallographic components of the MnP(I),P- to MnP(II),H_c-type transition in the $Cr_{1-t}T_tAs$ and $CrAs_{1-x}X_x$ phases are accomplished by adjustments of the unit-cell dimensions virtually alone. Hence, there appear to be degrees of crystallographic freedom which are relinquished (viz., constrained) during these transitions, and this sacrifice may hide valuable information on the origin of the crystallographic rearrangement.

The compositional variations in the unit-cell volume (V) of the $Cr_{1-t}T_tAs$ and $CrAs_{1-x}X_x$ phases at 10 K are depicted in Fig. 12.[1] The striking feature of the diagram is the significant distinction in unit-cell vol-

[1] During the preparation of Figs. 12 and 13 it became evident that the structural data for the H_c state of $CrAs_{0.95}P_{0.05}$ in (*9*) did not fit the general pattern for the other $Cr_{1-t}T_tAs$ and $CrAs_{1-x}X_x$ phases. At low-temperature powder X-ray diffraction examination of a fresh sample of $CrAs_{0.95}P_{0.05}$ revealed that an indexing mistake must have been made in the earlier work. The correct unit-cell dimensions at (say) 170 K are (in pm): a = 561.6(2), b = 358.4(2), and c = 614.2(2), which indeed are consistent with the other data in Figs. 12 and 13.

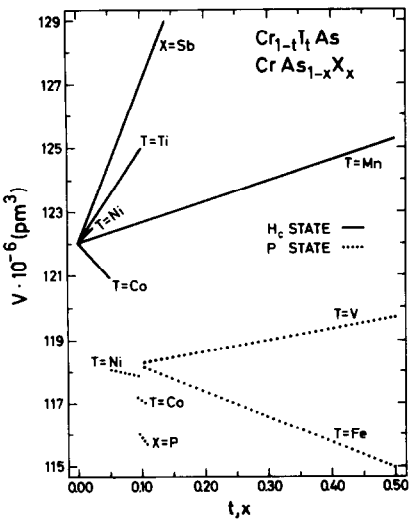

FIG. 12. Unit-cell volume (V) at 10 K (supplemented by data for 80 K) versus t or x for $Cr_{1-t}T_tAs$ and $CrAs_{1-x}X_x$. Legends are given in the illustration. Data from (*1, 3, 5–9*). (1 Å^3 = 10^6 pm^3.)

ume between the H_c- and P-type states. On extrapolation of the unit-cell volume of the P state to $t = x = 0.00$ (viz., to CrAs) $V_{10\,K} = 1.183 \times 10^6$ pm^3 is obtained as compared with $V_{10\,K} = 122.0 \times 10^6$ pm^3 for the H_c state, i.e., ~3% increase in $V_{10\,K}$ from the P to the H_c state.

A more varied picture of the structural properties which characterize the P and H_c states is provided in Fig. 13, which gives the variations in the three shortest T–T distances with t or x at 10 K. Also the T–T distances for the H_c and P states are seen to group themselves in pairs of separated distance intervals. On the other hand, no clear-cut distinction is found when the corresponding data for the average T–X distances are plotted as function of t or x. Extrapolation of the T–T distances for the P state at 10 K to $t = x = 0.00$ (viz., the Cr–Cr distances in the hypothetical P state of CrAs at 10 K) gives (in pm) $d_{1,4} = 289$, $d_{2,1} = 299$, and $d_{1,1} = 338$. These values are substantially different from those observed (*1*) both for the P state at 293 K [$d_{1,4}$ = 289.2(8), $d_{2,1}$ = 303.0(6), $d_{1,1}$ = 346.3(1) pm] and the H_c state at 80 K [$d_{1,4}$ = 284.9(7), $d_{2,1}$ = 306.4(5), and $d_{1,1}$ = 357.5(1) pm; which also should apply to 10 K; cf. Fig. 13]. Hence, the hypothetical P- to H_c-state transition of CrAs at 10 K would reduce $d_{1,4}$ by ~1.5% and increase $d_{2,1}$ and $d_{1,1}$ by ~2.5 and ~6%, respectively. The average Cr–As distance would, on the other hand, remain constant to an approximation better than 0.5% during such a transformation.

Since the T–T contacts play an important role as magnetic exchange interaction paths (in addition to indirect exchange *via* the X atoms) it seems natural to suspect that the (just mentioned) shortening of $d_{1,4}$ or extension of $d_{2,1}$ and/or $d_{1,1}$ could give some guidance concerning the magnetic component of the MnP(I),P- to MnP(II),H_c-type tran-

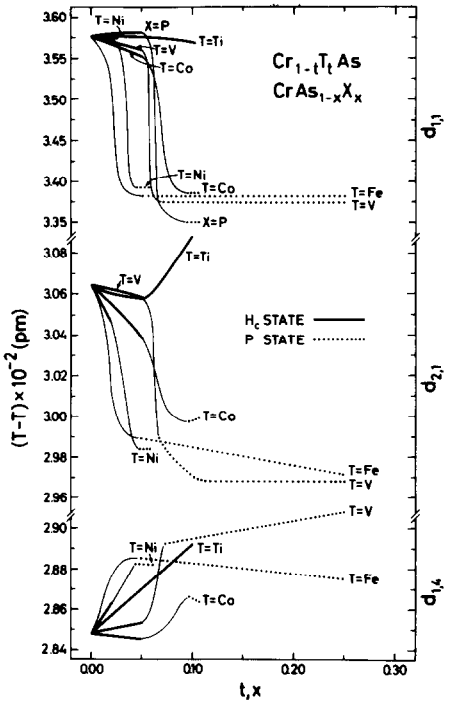

FIG. 13. Variations in the three shortest T–T distances of $Cr_{1-t}T_tAs$ and $CrAs_{1-x}X_x$ at 10 K (supplemented by data for 80 K), with t or x. Legends are given on the illustration. Data from (*1, 3, 5–9*). (1 Å = 10^2 pm.)

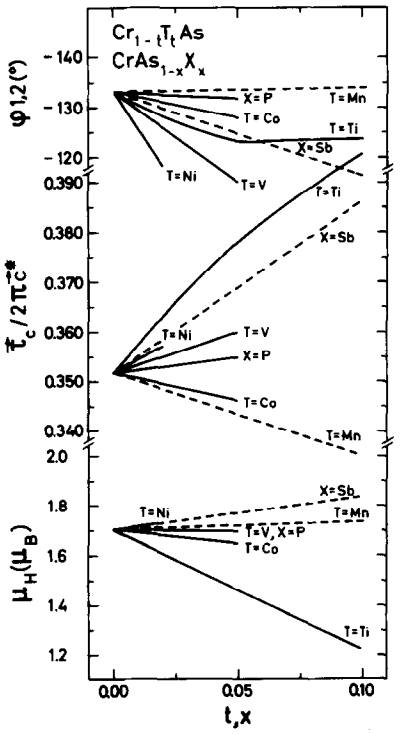

FIG. 14. Variations in μ_H, τ_c and $\phi_{1,2}$ as function of t or x for $Cr_{1-t}T_tAs$ and $CrAs_{1-x}X_x$. Curves for T = Mn and X = Sb are broken to emphasize that these refer to interpolation between $t = x = 0.00$ and $t = 0.60$ for T = Mn and $x = 0.14$ for X = Sb. Data from (*1*, *3–12*).

sition in $Cr_{1-t}T_tAs$ and $CrAs_{1-x}X_x$. The approximate constancy in the average T–X distance at the transition can almost certainly be regarded as a constraint which serves to minimize the free energy.

The compositional variations of the helimagnetic parameters μ_H, τ_c, and $\phi_{1,2}$ for $Cr_{1-t}T_tAs$ and $CrAs_{1-x}X_x$ at 10 K are shown in Fig. 14 (data for $T_{N,h}$ in Fig. 9). It appears that μ_H, τ_c, and $\phi_{1,2}$ undergo no spectacular changes over the stability ranges of the H_c mode. (Apart from a 30% reduction in μ_H from $t = 0.00$ to 0.10 for $Cr_{1-t}Ti_tAs$ the changes in μ_H, τ_c, and $\phi_{1,2}$ are within ±10% of the parameter value at $t = x = 0.00$.) Moreover, the changes that do occur in τ_c and $\phi_{1,2}$ are such that the approximately antiferromagnetic arrangement of the moments within the T–T zig-zag chains along the b axis (corresponding to the distance $d_{2,1}$) are retained from CrAs to $Cr_{1-t}T_tAs$ and $CrAs_{1-x}X_x$. On the basis of the variations in $T_{N,h}$ with t or x (Fig. 9) it seems likely that the (long-range) helimagnetic order breaks down because the overall magnetic exchange interaction (e.g., the linear combination of exchange parameters according to the molecular field approximation) ceases.

In line with the basis of Kallel *et al.* (*11*) (but without regarding the rest of their considerations) the exchange integrals $J_{1,4}$, $J_{2,1}$, $J_{1,1}$, and $J_{1,2}$ corresponding to the T–T distances $d_{1,4}$, $d_{2,1}$, $d_{1,1}$, and $d_{1,2}$, respectively, are believed to play a central role for the cooperative magnetic modes of the MnP-type phases. As seen from Fig. 13 the distinctions between the MnP(I),P- and MnP(II),H_c-type states are much more pronounced for $d_{2,1}$ and $d_{1,1}$, than for $d_{1,4}$. (The behavior of $d_{1,2}$ resembles a "mirror image" of $d_{2,1}$, but due to its long length $d_{1,2}$ probably corresponds to a relatively weak exchange interaction.) These findings led us to look for a possible correlation between $d_{2,1}$ and $d_{1,1}$ on the one hand and the occurrence of cooperative magnetism on the other. Figure 15 shows, e.g., data for binary and ternary MnP-type phases in a $d_{1,1}$-versus-$d_{2,1}/d_{1,1}$ diagram. (A certain selection has been made for ternary compositions which remain paramagnetic down to 10 K. The numbers in the figure refer to compositions listed in the legend.) Figure 15 is seen to provide some separation of the data points for compositions which adopt a cooperative magnetic state from those which remain paramagnetic. However, as emphasized by the shading the separation is certainly not sharp and such an empirical correlation represents a first, crude approximation. The fact that the points for the cooperative magnetic states occupy the upper right sector of Fig. 15

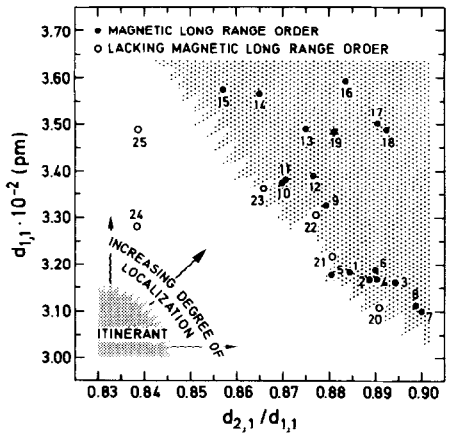

FIG. 15. $d_{1,1}$ versus $d_{2,1}/d_{1,1}$ for MnP-type phases which exhibit (●) or do not exhibit (○) long-range magnetic order. $d_{2,1}$ and $d_{1,1}$ are, respectively, the second and third shortest metal–metal distances of the MnP-type structure. (1) MnP, (2) $Mn_{0.80}V_{0.20}P$, (3) $Mn_{0.80}Cr_{0.20}P$, (4) $Mn_{0.80}Fe_{0.20}P$, (5) $Mn_{0.80}Co_{0.20}P$, (6) $Mn_{0.90}Ni_{0.10}P$, (7) FeP, (8) $FeP_{0.90}As_{0.10}$, (9) FeAs, (10) $Mn_{0.15}Fe_{0.85}As$, (11) $Cr_{0.25}Fe_{0.75}As$, (12) $Cr_{0.50}Fe_{0.50}As$, (13) $Mn_{0.70}Cr_{0.30}As$, (14) $Cr_{0.90}Ti_{0.10}As$, (15) CrAs, (16) $Cr_{0.60}Mn_{0.40}As$, (17) $Mn_{0.95}V_{0.05}As$, (18) $Mn_{0.90}Cr_{0.10}As$, (19) $Mn_{0.90}Fe_{0.10}As$, (20) CrP, (21) $FeAs_{0.50}P_{0.50}$, (22) $FeAs_{0.90}P_{0.10}$, (23) VAs, (24) CoP, and (25) CoAs. (1 Å = 10^2 pm.)

makes us place some confidence in the correlation because this would be consistent with a greater tendency for localized electron behavior in this part of the diagram. Moreover, it is also interesting to note that the MnP-type phases which take a cooperative state (viz., CrAs, MnP, "orthorhombic MnAs," FeP, and FeAs as well as their ternary derivatives) occupy different subsectors of Fig. 15, which in turn can be correlated with distinctions in their helimagnetic structures. On the other hand, a $d_{1,1}$-versus-$d_{2,1}/d_{1,1}$ plot does not provide an explanation of the crystallographic component of MnP(I),P- to MnP(II),H_c-type transition in CrAs and its ternary derivatives. The later negative finding is somewhat sad, because, after all, it was this problem which stimulated most of the present discussion!

References

1. K. SELTE, A. KJEKSHUS, W. E. JAMISON, A. F. ANDRESEN, AND J. E. ENGEBRETSEN, *Acta Chem. Scand.* **25,** 1703 (1971).
2. K. SELTE AND A. KJEKSHUS, *Acta Chem. Scand.* **27,** 3195 (1973).
3. K. SELTE, H. HJERSING, A. KJEKSHUS, AND A. F. ANDRESEN, *Acta Chem. Scand. A* **29,** 312 (1975).
4. N. KAZAMA AND H. WATANABE, *J. Phys. Soc. Japan* **30,** 1319 (1971).
5. H. FJELLVÅG AND A. KJEKSHUS, *Acta Chem. Scand.*, in press.
6. K. SELTE, H. FJELLVÅG, A. KJEKSHUS, AND A. F. ANDRESEN, *Acta Chem. Scand. A* **33,** 727 (1979).
7. K. SELTE, A. KJEKSHUS, S. AABY, AND A. F. ANDRESEN, *Acta Chem. Scand. A* **29,** 810 (1975).
8. I. L. A. DELPHIN, K. SELTE, A. KJEKSHUS, AND A. F. ANDRESEN, *Acta Chem. Scand. A* **32,** 179 (1978).
9. K. SELTE, H. HJERSING, A. KJEKSHUS, A. F. ANDRESEN, AND P. FISCHER, *Acta Chem. Scand. A* **29,** 695 (1975).
10. H. BOLLER AND A. KALLEL, *Solid State Commun.* **9,** 1699 (1971).
11. A. KALLEL, H. BOLLER, AND E. F. BERTAUT, *J. Phys. Chem. Solids* **35,** 1139 (1974).
12. H. FJELLVÅG AND A. KJEKSHUS. *Acta Chem. Scand. A* **38,** 1 (1984).
13. H. WATANABE, N. KAZAMA, Y. YAMAGUCHI, AND M. OHASHI, *J. Appl. Phys.* **40,** 1128 (1969).
14. N. KAZAMA AND H. WATANABE, *J. Phys. Soc. Japan* **31,** 943 (1971).
15. R. BLACHNIK, G. KUDERMANN, F. GRØNVOLD, A. ALLES, B. FALK, AND E. F. WESTRUM, *J. Chem. Thermodyn.* **10,** 507 (1978).
16. H. BOLLER AND H. NOWOTNY, *Monatsh. Chem.* **96,** 852 (1965).
17. R. SOBEZAK, H. BOLLER, AND H. BITTNER, *Monatsh. Chem.* **99,** 2227 (1968).
18. A. ZIEBA, H. FJELLVÅG, AND A. KJEKSHUS, *J. Phys. Chem. Solids* **46,** 275 (1985).
19. R. D. DESLATTERS AND A. HENINS, *Phys. Rev. Lett.* **31,** 972 (1973).
20. A. W. HEWAT, "The Rietveld Computer Program for the Profile Refinement of Neutron Diffraction Powder Patterns Modified for Anisotropic Thermal Vibrations," UKAERE Harwell Report RRL 73/897 (1973).
21. H. M. RIETVELD, *J. Appl. Crystallogr.* **2,** 65 (1968).
22. The Neutron Diffraction Commission (1976).
23. R. E. WATSON AND A. J. FREEMAN, *Acta Crystallogr.* **14,** 27 (1961).
24. A. KJEKSHUS AND W. B. PEARSON, *Prog. Solid State Chem.* **1,** 83 (1964).

25. H. F. FRANZEN, C. HAAS, AND F. JELLINEK, *Phys. Rev. B* **10,** 1248 (1974).
26. K. SELTE, A. KJEKSHUS, AND A. F. ANDRESEN, *Acta Chem. Scand.* **27,** 3607 (1973).
27. K. SELTE, A. KJEKSHUS, G. VALDE, AND A. F. ANDRESEN, *Acta Chem. Scand. A* **30,** 468 (1976).
28. K. SELTE, A. KJEKSHUS, G. VALDE, AND A. F. ANDRESEN, *Acta Chem. Scand. A* **30,** 8 (1976).
29. T. SUZUKI AND H. IDO, *J. Phys. Soc. Japan* **51,** 3149 (1982).
30. J. B. GOODENOUGH, D. H. RIDGLEY, AND W. A. NEWMAN, *in* "Proceedings, International Conference on Magnetism, Nottingham," p. 542 (1964).
31. L. R. EDWARDS AND L. C. BARTEL, *Phys. Rev. B* **5,** 1064 (1972).
32. K. SELTE, H. FJELLVÅG, AND A. KJEKSHUS, *Acta Chem. Scand. A* **33,** 391 (1979).
33. K. SELTE, A. KJEKSHUS, AND A. F. ANDRESEN, *Acta Chem. Scand. A* **28,** 61 (1974).
34. H. FJELLVÅG, K. SELTE, AND F. E. STAVE, *Acta Chem. Scand. A* **38,** 687 (1984).
35. H. FJELLVÅG AND A. KJEKSHUS, to be published.
36. P. G. FELCHER, *J. Appl. Phys.* **37,** 1056 (1966).
37. J. B. FORSYTH, S. J. PICKART, AND P. J. BROWN, *Proc. Phys. Soc.* **88,** 333 (1966).
38. A. KJEKSHUS AND W. E. JAMISON, *Acta Chem. Scand.* **25,** 1715 (1971).